Parallel acoustic near-field microscope: A steel slab with a periodic array of slits

Fengming Liu, Feiyan Cai, Shasha Peng, Rui Hao, Manzhu Ke, and Zhengyou Liu*
Key Laboratory of Acoustic and Photonic Materials and Devices of Ministry of Education and Department of Physics, Wuhan University, Wuhan 430072, People's Republic of China
(Received 4 May 2009; published 17 August 2009)

We propose a practical acoustic near-field microscope, which is simply a steel slab with periodic array of subwavelength slits. The near field is transported by the coupling of the incident evanescent waves and the acoustic guided modes supported by the structured slab. The transmission coefficients of the structured slab as a function of the transverse wave vector are theoretically derived, and a theoretical model is employed to study the imaging of the proposed device. Numerical simulations are also performed to verify the theoretical results, which show that subwavelength imaging with good quality can indeed be realized.

DOI: 10.1103/PhysRevE.80.026603 PACS number(s): 43.20.+g, 43.35.+d, 43.40.+s

Negative refraction and subwavelength imaging in electromagnetic waves have attracted a great interest in the scientific community since Pendry proposed a "perfect lens" making a perfect image without any deterioration [1]. Several approaches such as left-handed material with negative permittivity and permeability [2–5], dielectric-based photonic crystals [6–11], anisotropic layered structures with effective permittivity tensor [12–14], and canalization using an array of metallic wires [15–17] have been reported for restoring evanescent waves so as to overcome the diffraction limit.

Recently, the concept of negative refraction and imaging effect has been generalized to acoustic waves. In particular, phononic crystals have been widely exploited to achieve focusing of acoustic waves. It has been shown that there are two kinds of schemes of using phononic crystals. One is in the low frequency region, where the wavelength in this range is very large compared to the lattice constant. For such a case, phononic crystals can be treated as homogeneous materials, and therefore they can be used to design acoustics lens with curve shape in analogy with normal lens [18,19]. The other way is through negative refraction in the first or second bands of phononic crystal slabs [20–25]. However, no evidence of true realization of subwavelength imaging has been presented in the aforementioned works. We also note that in the latest paper [26], Sukhovich *et al.* demonstrated both theoretically and experimentally the achievement of imaging with super-resolution using a phononic crystals lens via the excitation of bound slab modes. However, in their work, the appearance of strong peaks flanking the image peak makes it difficult to distinguish the image from the background. As already shown in Ref. [8], this image field pattern may not be good enough for imaging purpose. In addition to phononic crystals, acoustic metamaterials were also reported for achieving focusing of acoustic waves [27,28]. Although it was theoretically demonstrated that the lens constituted of acoustic metamaterials can indeed overcome the diffraction limit, the fabrication of such materials seems impracticable so far.

In our recent work [29], it was shown that a steel slab with periodic array of subwavelength slits may serve as a material of tunable refractive index (thus can be high as required) for airborne sound. In the present paper, we will further demonstrate that the structured slab can support acoustic guided modes. By coupling with these guided modes, the near field of the source can be transported through the structured slab. Therefore, the structured slab is capable of serving as an acoustic near-field microscope, which can transfer an image with subwavelength resolution from the front surface of the microscope to the back surface. Although our near-field microscope has to be placed in the close region of the source to capture evanescent waves, the thickness of the microscope could be much larger than the wavelength of operation as long as the thickness fulfills the Fabry-Pérot resonance condition at that wavelength. Hence, the acoustic near-field microscope may also be regarded as an acoustic endoscope which can transport images with subwavelength resolution for a rather long distance. Moreover, it is worth noting that, compared with the previously mentioned acoustic metamaterials, our structured slab is much simpler to design and fabricate, while compared to the scheme of Sukhovich *et al.*, our proposed device can obtain an image with better quality.

The geometry of the proposed acoustic near-field microscope, consisted of a steel slab with periodically arrayed cut-through slits placed in air, is illustrated in Fig. 1. The width of the slit, the grating period, and the slab thickness are denoted by a, d, and h, respectively; throughout the whole paper $a=0.1d$ and $h=4d$ are set as an example. Moreover,

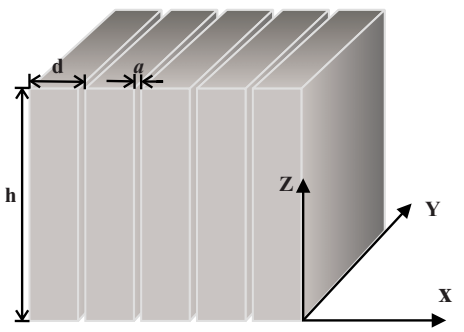

FIG. 1. (Color online) Schematic of the steel slab with periodic array of subwavelength slits.

*Author to whom all correspondence should be addressed; zyliu@whu.edu.cn

we regard the steel slab as perfect rigid body for the huge acoustic impedance mismatch between steel and air, $Z_{steel}/Z_{air} \approx 110\,789$.

To begin with, we derive the analytical formulas which describe the transmission through the slab and the dispersion relation of the guided modes. The analytical formulas are based on a model expansion of the pressure fields in the different regions defining the structure. The pressure fields inside the mth slit, above the slab and below the slab, have the following forms:

$$P^m(x,z) = a^m e^{ikz} + b^m e^{-ik(z-h)} \quad \text{for } |x - md| \le a/2, \quad (1)$$

$$P^{above}(x,z) = \sum_p (\delta_{0,p} e^{i\alpha_p z} + r_p e^{-i\alpha_p z}) e^{iG_p x}, \quad (2)$$

$$P^{below}(x,z) = \sum_p t_p e^{i\alpha_p (z-h)} e^{iG_p x}, \quad (3)$$

where a^m and b^m are the corresponding amplitudes of the forward and backward guiding waves in the slit, $k=\omega/c$ is the momentum of acoustic waves in air (ω is the frequency and c is the sound velocity), $\delta_{0,p}$ is the Kronecker delta, r_p and t_p are the normalized pressure field amplitudes of the pth reflected- and transmitted-diffracted waves, $G_p = k_x + 2\pi p/d$ is the parallel momentum along the slab surface of the pth diffraction order, with k_x being the x component of the incident wave vector, and $\alpha_p = \sqrt{k^2 - G_p^2}$ is the momentum of the pth diffraction order field external to the slab in the z direction. The velocity fields are then obtained from $\rho \partial V_q/\partial t = -\partial P/\partial q (q = x, z)$, where ρ is the mass density of air. It should be noted that, inside the slit, only the zero-order guiding mode has been considered for the width of the slit that is much smaller than the wavelength. By requiring continuity of V_z and p at the interfaces over the slit region, vanishing V_z elsewhere on the interface at $z=0$ and $z=h$, we obtain the transmission amplitude for the pth diffraction order,

$$t_p = \frac{4fkug_p}{[(1+\phi)^2 - (1-\phi)^2 u^2]\alpha_p}, \quad (4)$$

where $u \equiv e^{ikh}$ is the phase accumulation across the thickness h, $f \equiv a/d$ is the area filling factor of the slits, $g_p \equiv \mathrm{sinc}(G_p a/2)$, and $\phi = fk\Sigma_{p=-\infty}^{\infty}(g_p^2/\alpha_p)$. As reported in Ref. [29], the structured slab can be approximated as a homogeneous material with high effective refractive index due to the similar of the transmission properties between them. One knows that a high-index homogeneous slab can support guided mode along it. Thus, it is reasonable for us to consider that the structured slab may also support some guided mode. Note that, for the periodicity of the slits that is much smaller than the wavelength of airborne sound, all diffraction orders are evanescent in the z direction, which can be revealed in the expression for α_p. When these diffraction waves couple with each other, guided modes propagating along the transverse direction of the structured slab are built up. We note that in Ref. [30] an acoustic mode guided along a plate of perfect rigid body drilled with slits was presented. Although the author considered that the guided mode was originated from strongly coupled surface modes in that work, we believe that it shares the identical mechanism with ours here. The dispersion relation of the guided modes can be solved by using Eqs. (1)–(3) but without the term corresponding to the incident wave. The even modes satisfy the dispersion relation

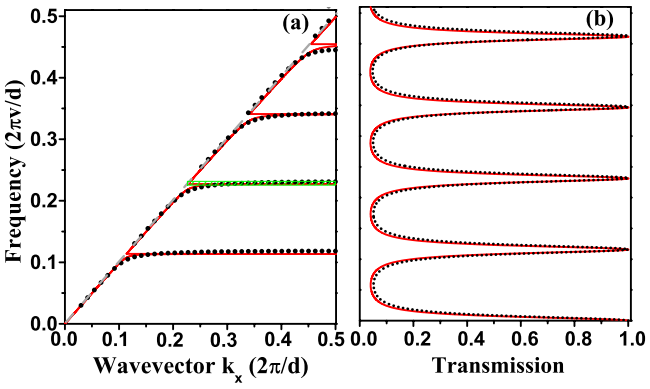

FIG. 2. (Color online) (a) Dispersion relation of the acoustic guided modes. The quantity v is sound velocity in air. Green bar denotes the frequencies of operation. Dashed line: the sound line. (b) The normal-incidence transmission spectrum of the structured slab. In both figures: solid red lines represent the results obtained via the analytical formula; dotted black lines represent the results obtained via the FDTD method.

$$\frac{1}{i\phi} = \tan\left(\frac{\omega h}{2c}\right) \quad (5)$$

and the odd modes satisfy the dispersion relation

$$\frac{1}{i\phi} = -\cot\left(\frac{\omega h}{2c}\right), \quad (6)$$

as calculated by applying the continuity of V_z and p on the interface at $z=0$ and $z=h$. Figure 2 shows the dispersion relation of the guided modes in the first Brillouin zone of the structured slab and the transmission amplitude of normal incidence. The guided modes start form a linear part close to the propagation cone of sound, while at large transverse wave vector, they approach the frequencies corresponding to the transmittance peaks. In Fig. 2, the solid red lines represent the results calculated with the analytical formula, whereas the dotted black lines represent the results calculated with the finite-difference time-domain (FDTD) method [31]. As seen, the analytical model is in good agreement with the FDTD simulation. In the following section, we will demonstrate that the guided modes play a key role in enhancing evanescent waves.

We calculate the transmission coefficients of the structured slab as a function of the transverse wave vector k_x for different frequencies close to the second transmittance peaks using Eq. (4). The transmission coefficient can be regarded as the transfer function $T(\omega, k_x)$ of the structured slab: the spatial Fourier components of the image field at the output plane can be obtained via multiplying that of the source field at the input plane by $T(\omega, k_x)$. Here, only the transmissions for the zeroth and first diffraction orders are considered for $T(\omega, k_x)$ since the higher-order transmissions are much

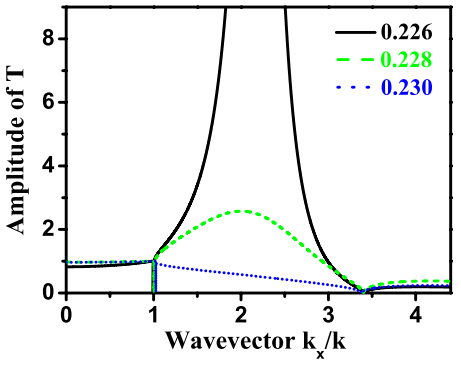

FIG. 3. (Color online) Amplitude of the transmission coefficient as a function of the normalized transverse wave vector k_x for different frequencies of operation.

smaller and thus can be neglected. In Fig. 3, the amplitude of $T(\omega,k_x)$ for different frequencies of operation is plotted. It is seen that the behavior of $T(\omega,k_x)$ is sensitive to variations in the frequency of operation. For $\omega=0.226(2\pi v/d)$, the operation frequency is within the frequency range of the flat guided mode band. At the range of wave vectors of evanescent waves, a resonant peak appears which indicates the excitation of guided mode. As increasing ω to $0.228(2\pi v/d)$, the frequency is beyond the range of the guided mode band. However, as analyzed in Ref. [8], evanescent waves are still amplified as long as the frequency is sufficiently close to the guided mode band. As seen, the amplification of evanescent waves is moderate in this case. While further increasing frequency of operation, the frequency deviates further from the guided mode band. Therefore, less and less evanescent waves can be amplified, and the amplitude of $T(\omega,k_x)$ is eventually less than unity at the evanescent wave range. Consequently, for certain range of frequency, the result shown in Fig. 3 confirms our expectation that the guided modes below the sound line result in amplification of evanescent waves.

We now study the imaging properties of the proposed device considering the characteristic of $T(\omega,k_x)$ calculated above. An ideal point source $S(k_x)$, which has uniform spatial spectrum for propagating waves and evanescent waves, is placed at a distance $d_1=0.25d$ before the device. It is straightforward to obtain the image intensity I_{image} at a distance $d_2=0.25d$ behind the device,

$$I_{image}(x)=\left|A_0\int e^{-\sqrt{k_x^2-k^2}(d_1+d_2)}T(\omega,k_x)S(k_x)e^{-ik_xx}dk_x\right|^2. \tag{7}$$

In Eq. (7), A_0 is a constant defining the amplitude of the source, $e^{-\sqrt{k_x^2-k^2}(d_1+d_2)}$ represents the transfer function for a slab of free space with $d_1+d_2=0.5d$ thickness, and $T(\omega,k_x)$ is the transfer function of the proposed device.

As already shown in Fig. 3, for the different frequencies of operation near the guided mode band, although the transmission for propagating waves is nearly the same, there are large differences in the transmission of evanescent waves. In order to derive the optimal frequency to obtain the appropriate amplification of evanescent waves, we compare the transmission of our proposed device with that of the perfect lens formed by acoustic metamaterials with refractive index $n=-1$. As can be seen in Fig. 4(a), a slab of acoustic metamaterials with $d_1+d_2=0.5d$ thickness is capable of completely making up the decay of evanescent waves in free space with the identical thickness; therefore the total transmission coefficient equals unity for any wave vector k_x. In Fig. 4(b), the total transmission coefficient of our proposed structure for the frequency $\omega=0.226(2\pi v/d)$ is presented. In this case, the total transmission coefficient deviates significantly from that of the perfect lens. This indicates that evanescent waves are amplified excessively, and thus the image pattern will be dominated by evanescent waves, which is undesirable for imaging purpose. For $\omega=0.228(2\pi v/d)$ [Fig. 4(c)], the total transmission coefficient is close to unity for $k_x/k<1.8$. Although the range of wave vector for the amplified transmission is limited, evanescent waves are amplified moderately within this range. Consequently, a subwavelength image with good quality may be obtained. Using the Eq. (7), we calculate the image intensity I_{image} for the different frequencies of operation, which confirms our above analysis. In Fig. 5, the normalized image intensity I_{image} at the image plane is plotted as a function of x/d. Intensity maximum at $x=0$ can be observed for both frequencies, and the transverse x size of the intensity peak of $\omega=0.226(2\pi v/d)$ (solid black line) is clearly smaller than that of $\omega=0.228(2\pi v/d)$ (dashed green line). As shown in Ref. [8], this indicates that larger range of wave vectors of amplified evanescent waves has been included in the subwavelength imaging for the case of $\omega=0.226(2\pi v/d)$. However, strong intensity peaks simultaneously occur alongside the main intensity peak, and the image becomes indistinguishable against this strong background, which is undesirable for imaging purposes. In con-

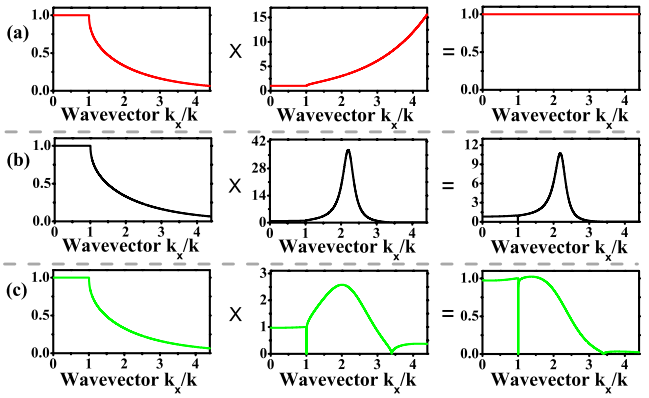

FIG. 4. (Color online) Comparison of transmission characteristics of different types of imaging devices. (a) The perfect lens formed by acoustic metamaterials with refractive index $n=-1$. (b) The proposed acoustic near-field microscope for the frequency of operation $\omega=0.226(2\pi v/d)$. (c) The proposed acoustic near-field microscope for the frequency of operation $\omega=0.228(2\pi v/d)$. Left column: transmission coefficient as a function of the normalized transverse wave vector k_x for $d_1+d_2=0.5d$ thick slab of free space. Medium column: transmission coefficient of acoustic metamaterial lens and that of the structured slab for the different frequencies of operation. Right column: total transmission coefficient.

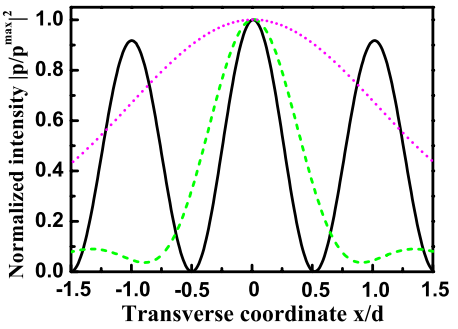

FIG. 5. (Color online) The normalized intensity distribution of the image as a function of x/d. Solid black line: for $\omega=0.226(2\pi v/d)$. Dashed green line: for $\omega=0.228(2\pi v/d)$. Dotted magenta line: the normalized intensity at the image plane when the proposed acoustic near-field microscope is removed.

trast to $\omega=0.226(2\pi v/d)$, a distinct intensity peak appears against the background in the case of $\omega=0.228(2\pi v/d)$. The transverse x size of this intensity peak is equal to 0.41λ, which is much smaller than the diffraction limit λ. In Fig. 5, we also depict the normalized intensity at the image plane when the proposed acoustic near-field microscope is removed (dotted magenta line). For the propagating distance $d_1+d_2+h=4.5d$ between the source and the image plane and the rapid decay of evanescent waves in free space, the transverse x size of the intensity peak is close to the diffraction limit λ. Therefore, we have shown that subwavelength imaging with good quality using the proposed acoustic near-field microscope can be achieved indeed.

In addition, we have studied the imaging properties of the proposed acoustic near-field microscope using the FDTD method. Here, the width of the structured slab along x is limited ($40d$) in the simulation. The field distributions of pressure are plotted in Figs. 6(a) and 6(b) for the frequencies $\omega=0.226$ and $0.228(2\pi v/d)$, respectively. As can be seen in Fig. 6(a), the guided mode is excited; the pressure fields propagate along the transverse direction and decay exponentially away from the slab in the z direction. Due to this strong field distribution of pressure close to the surfaces of the slab, the image is undistinguished. Whereas, a clear image with good quality is presented in Fig. 6(b), which is ideal for imaging purposes. Note that the effects of reflection are inconspicuous because the frequency of operation is close to the transmittance peaks. Finally, we compare the normalized image intensity I_{image} calculated using FDTD method with that using theoretical model in Fig. 6(c); the agreement is quite satisfactory.

We have found that, for the guided mode bands are close with the Fabry-Pérot resonance frequencies, the proposed devices with different thicknesses will obtain almost identical images if only the thicknesses equal an integer number of half-wavelengths. We have also found that, by further optimizing the frequency of operation, the ultimate resolution of the device can reach the grating period d, which is consistent

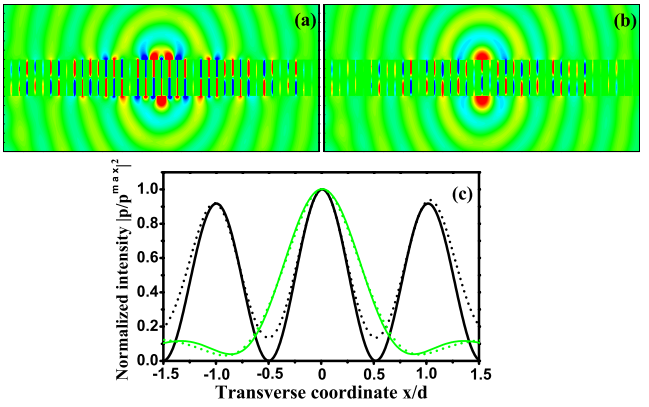

FIG. 6. (Color online) The pressure field distributions of imaging by the proposed acoustic near-field microscope calculated using FDTD simulation: (a) for $\omega=0.226(2\pi v/d)$; (b) for $\omega=0.228(2\pi v/d)$. In both cases, the point source is located at the bottom side of the device. (c) The normalized intensity distribution of the image for both frequencies calculated using theoretical model (solid lines) and using FDTD method (dotted lines), respectively.

with that the resolution of periodic structure is limited by its period [8,16]. Therefore, we can improve the resolution of the device just by decreasing the grating period. At last, we have calculated the transfer function of the structured slab as a function of k_x with considering absorption. We found that the transfer function does not change obviously at audible frequencies for sound in air, with the typical value of the absorption being less than 10^{-3} order of magnitude. Therefore, the imaging effect is not sensitive to absorption at audible frequencies.

In conclusion, we have investigated the imaging property of an acoustic near-field microscope constituted of a steel slab with periodic array of slits. It is shown that the structured slab can support acoustic guided modes, which can be exploited to enhance evanescent waves. We present analytical formula that describes the transmission of the structured slab. By slightly tuning the frequencies of operation, the transmission coefficients alter significantly, which results in remarkable changes in the image patterns correspondingly. Using the theoretical model and the FDTD simulation, it is shown that subwavelength image with good quality can indeed be obtained. We note that, in fact, the mechanism which we exploit here to obtain subwavelength imaging is somehow analogous to that presented in Ref. [32], where a metamaterial characterized by high index of refraction and confined guided modes was used to achieve subwavelength imaging in electromagnetic waves. Since our proposed device is very simple to fabricate, we hope that this work would stimulate more interests of experimental research in the acoustic subwavelength imaging.

This work was supported by the National Natural Science Foundation of China (Grants No. 10874131, No. 10731160613, No. 50425206, and No. 50702038).

[1] J. B. Pendry, Phys. Rev. Lett. **85**, 3966 (2000).
[2] A. A. Houck, J. B. Brock, and I. L. Chuang, Phys. Rev. Lett. **90**, 137401 (2003).
[3] A. Grbic and G. V. Eleftheriades, Phys. Rev. Lett. **92**, 117403 (2004).
[4] A. N. Lagarkov and V. N. Kissel, Phys. Rev. Lett. **92**, 077401 (2004).
[5] N. Fang, H. Lee, C. Sun, and X. Zhang, Science **308**, 534 (2005).
[6] C. Luo, S. G. Johnson, J. D. Joannopoulos, and J. B. Pendry, Phys. Rev. B **65**, 201104(R) (2002).
[7] E. Cubukcu, K. Aydin, E. Ozbay, S. Foteinopoulou, and C. M. Soukoulis, Phys. Rev. Lett. **91**, 207401 (2003).
[8] C. Luo, S. G. Johnson, J. D. Joannopoulos, and J. B. Pendry, Phys. Rev. B **68**, 045115 (2003).
[9] P. V. Parimi, W. T. Lu, P. Vodo, and S. Sridhar, Nature (London) **426**, 404 (2003).
[10] A. Berrier, M. Mulot, M. Swillo, M. Qiu, L. Thylén, A. Talneau, and S. Anand, Phys. Rev. Lett. **93**, 073902 (2004).
[11] R. Chatterjee, N. C. Panoiu, K. Liu, Z. Dios, M. B. Yu, M. T. Doan, L. J. Kaufman, R. M. Osgood, and C. W. Wong, Phys. Rev. Lett. **100**, 187401 (2008).
[12] Z. Jacob, L. V. Alekseyev, and E. Narimanov, Opt. Express **14**, 8247 (2006).
[13] A. Salandrino and N. Engheta, Phys. Rev. B **74**, 075103 (2006).
[14] Z. Liu, H. Lee, Y. Xiong, C. Sun, and X. Zhang, Science **315**, 1686 (2007).
[15] P. A. Belov, Y. Hao, and S. Sudhakaran, Phys. Rev. B **73**, 033108 (2006).
[16] P. A. Belov and M. G. Silveirinha, Phys. Rev. E **73**, 056607 (2006).
[17] G. Shvets, S. Trendafilov, J. B. Pendry, and A. Sarychev, Phys. Rev. Lett. **99**, 053903 (2007).
[18] F. Cervera, L. Sanchis, J. V. Sanchez-Perez, R. Martinez-Sala, C. Rubio, F. Meseguer, C. Lopez, D. Caballero, and J. Sanchez-Dehesa, Phys. Rev. Lett. **88**, 023902 (2001).
[19] B. C. Gupta and Z. Ye, Phys. Rev. E **67**, 036603 (2003).
[20] S. Yang, J. H. Page, Z. Liu, M. L. Cowan, C. T. Chan, and P. Sheng, Phys. Rev. Lett. **93**, 024301 (2004).
[21] X. D. Zhang and Z. Y. Liu, Appl. Phys. Lett. **85**, 341 (2004).
[22] M. Z. Ke, Z. Y. Liu, C. Y. Qiu, W. G. Wang, J. Shi, W. J. Wen, and P. Sheng, Phys. Rev. B **72**, 064306 (2005).
[23] L. Feng, X. P. Liu, M. H. Lu, Y. B. Chen, Y. F. Chen, Y. W. Mao, J. Zi, Y. Y. Zhu, S. N. Zhu, and N. B. Ming, Phys. Rev. Lett. **96**, 014301 (2006).
[24] M. H. Lu *et al.*, Nature Mater. **6**, 744 (2007).
[25] A. Sukhovich, L. Jing, and J. H. Page, Phys. Rev. B **77**, 014301 (2008).
[26] A. Sukhovich, B. Merheb, K. Muralidharan, J. O. Vasseur, Y. Pennec, P. A. Deymier, and J. H. Page, Phys. Rev. Lett. **102**, 154301 (2009).
[27] M. Ambati, N. Fang, C. Sun, and X. Zhang, Phys. Rev. B **75**, 195447 (2007).
[28] X. Ao and C. T. Chan, Phys. Rev. E **77**, 025601(R) (2008).
[29] F. Y. Cai, F. M. Liu, Z. J. He, and Z. Y. Liu, Appl. Phys. Lett. **91**, 203515 (2007).
[30] J. Christensen, L. Martin-Moreno, and F. J. Garcia-Vidal, Phys. Rev. Lett. **101**, 014301 (2008).
[31] A. Taflove, *Computational Electrodynamics: The Finite-Difference Time-Domain Method* (Artech House, Norwood, 2000).
[32] M. G. Silveirinha, C. A. Fernandes, and J. R. Costa, Phys. Rev. B **78**, 195121 (2008).